

The stellar population associated with the IRAS source 16132-5039 ¹

A. Roman-Lopes, Z. Abraham

*Instituto de Astronomia, Geofísica e Ciências Atmosféricas, Universidade de São Paulo
Rua do Matão 1226, 05508-900, São Paulo, SP, Brazil*

roman@astro.iag.usp.br

ABSTRACT

We report the discovery of a young massive stellar cluster and infrared nebula in the direction of the CS molecular cloud associated to the IRAS point source 16132-5039. The analysis of the mid-infrared images from the more accurate MSX catalog, revealed that there are two independent components associated with the IRAS source. The integral of the spectral energy distribution for these components, between $8.28 \mu\text{m}$ and $100 \mu\text{m}$, gave lower limits for the bolometric luminosity of the embedded objects of $8.7 \times 10^4 L_{\odot}$ and $9 \times 10^3 L_{\odot}$, which corresponds to ZAMS O8 and B0.5 stars, respectively. The number of Lyman continuum photons expected from the stars that lie along the reddening line for early-type stars is about $1.7 \times 10^{49} \text{ s}^{-1}$, enough to produce the detected flux densities at 5 GHz. The NIR spectrum of the nebula increases with frequency, implying that free-free emission cannot be the main source of the extended luminosity, from which we conclude that the observed emission must be mainly dust scattered light. A comparison of the cluster described in this paper with the young stellar cluster associated with the IRAS source 16177-5018, which is located at the same distance and direction, shows that the mean visual absorption of the newly discovered cluster is about 10 magnitudes smaller and it contains less massive stars, suggesting that it was formed from a less massive molecular cloud.

Subject headings: stars : formation – stars: pre-main sequence – infrared : stars – ISM: HII regions – ISM: dust, extinction

1. Introduction

Massive stars are born within dense molecular clouds forming clusters and associations; during their formation and early evolution they are often visible only at infrared and radio wavelengths. With the advent of the large bidimensional near-infrared array detectors, the morphological and photometric studies of extremely young galactic stellar clusters have benefited. At near-infrared wavelengths (1 to $2.5 \mu\text{m}$) it is possible to probe deep into the dense dust clouds where star formation is taking place.

The strong ultraviolet (UV) radiation emitted by the massive stars dissociates and ionizes the

gas, forming compact HII regions seen at radio wavelengths. A large fraction of the radiation could also heat the dust, which eventually radiates in the far-infrared (FIR); for this reason, compact HII regions are among the brightest and most luminous objects in the Galaxy at $100 \mu\text{m}$.

Because massive stars evolve very fast, they are extremely rare and difficult to find, except when related to the emission of the surrounding molecular cloud. In that sense, CS and NH_3 lines at radio frequencies, characteristic of high density gas, are good tracers of massive star forming regions.

In this paper we present observations in the near infrared, of a young stellar cluster of massive stars in the direction of the IRAS point source I16132-5039. This work is a part of a survey aimed to the identification of stellar pop-

¹Based on observations made at Laboratório Nacional de Astrofísica/MCT, Brazil

ulations in the direction of IRAS sources that have colors characteristics of ultracompact HII regions (Wood & Churchwell 1989) and strong CS (2-1) line emission (Bronfman et al. 1996). The studied region is located in the direction of another massive star forming region associated to the IRAS point source 16177-5018 (Roman-lopés et al. 2003); they are part of the RCW 106 complex, located in the southern Galactic plane at a distance of 3.7 kpc (Caswell & Haynes 1987). The near-infrared cluster presented here had recently been located by Dutra et al. (2003) by visual inspection of the 2MASS images; however their work contains only the possible cluster location, and as Persi, Tapia & Roth (2000) already showed for NGC6334IV, a high concentration of K band sources can be due to localized low extinction and be mistaken with a stellar cluster, leading to false identifications.

The cluster is associated with the radio source 332.541-0.111, which presents continuum radio emission at 5 GHz as well as hydrogen recombination lines (Caswell & Haynes 1987). The observations and data reduction are described in section 2, the results are presented in section 3 and our main conclusions are summarized in section 4.

2. Observations and data reduction

The imaging observations were performed in June 2001 and May 2003 with the Near Infrared Camera (CamIV) of Laboratório Nacional de Astrofísica (LNA), Brazil, equipped with a Hawaii 1024x1024 pixel HgCdTe array detector mounted on the 0.6 m Boller & Chivens telescope. The observations consisted of 8'x 8' frames in the direction of the IRAS source 16132-5039; the plate scale was 0.47 arcsec/pixel and the mean values of the PSF full width at half maximum (FWHM) were 1.4, 1.7 and 2.1 arcsec at the J , H and nbK images. The total integration time was 2220 s for J , 1440 s for H and 6400 s for nbK filters, resulting in a sensitivity at 3σ of 18.2, 17.4 and 14.2 magnitudes and completeness limits of 17.8, 16.5 and 13.8 magnitudes respectively. Details about the calibration and reduction procedures can be found in Roman-Lopés et al. (2003).

Photometry from 2MASS All Sky Point Source

Catalogue ² in the J , H and K_S filters became available recently, with completeness limits of 15.8, 15.1 and 14.3 magnitudes, in the three passbands (Egan et al. 2001). Since the 2MASS K_S band photometry, centered at 2.17 μm and with a bandpass of 0.32 μm has a completeness limit greater than our nbK photometry, we completed our observations with the 2MASS catalogue astrometry and magnitudes in this filter. The comparison of our photometry with the 2MASS survey data, in an area of about 40 square arcmin, corresponding to a total of 469, 610 and 440 common sources in the J , H and K bands, respectively, is shown in figure 1. We see a good linear relation between the two systems, with a slope of 1 and a dispersion that increases with the magnitude.

3. Results & Discussion

The combined false-colour infrared image, (J blue, H green and nbK red) of the whole field is displayed in Figure 2, together with amplified individual images of the nebular region at all bands. All of them, but especially the H and nbK images, shows the presence of a small spheroidal nebula with a bright star at its center.

3.1. The IRAS source

In Figure 3 we present a contour map constructed from the LNA nbK image, with a beam size of 2×2 pixels which shows the region around IRAS16132-5039. The contours start at 2.2×10^{-4} Jy/beam and are spaced by this same value. The IRAS coordinate has an intrinsic error delimited by the ellipse plotted in the figure. A more accurate position for the IR source was obtained from the Midcourse Space Experiment - MSX point source catalog (psc) ³. The MSX surveyed the entire Galactic plane within $|b| \leq 5^\circ$ in four mid-infrared spectral bands centered at 8.28, 12.13, 14.65 and 21.34 μm , with image resolution of 19 arcsec and a global absolute astrometric accuracy of about 1.9 arcsec (Price et al. 2001). We found one MSX source, with coordinates $\alpha(\text{J2000}) = 16^{\text{h}}17^{\text{m}}02.47^{\text{s}}$, $\delta(\text{J2000}) = -50^{\text{d}}47^{\text{m}}03.5^{\text{s}}$ within the IRAS uncertainty ellipse; its coordinates coincides with the star we labeled IRS1.

²<http://www.ipac.caltech.edu/>

³<http://www.ipac.caltech.edu/ipac/msx/msx.html>

However, looking at the MSX images, we found another closeby source, although outside the IRAS uncertainty ellipse, with coordinates $\alpha(\text{J2000}) = 16^{\text{h}}16^{\text{m}}55.94^{\text{s}}$, $\delta(\text{J2000}) = -50^{\text{d}}47^{\text{m}}07.8^{\text{s}}$. In Figure 4 we present our H band image overlaid with the $8.28\mu\text{m}$ band MSX contour diagram, with the contours spaced by $8 \times 10^{-6} \text{ W m}^{-2} \text{ sr}^{-1}$, starting at $2.8 \times 10^{-5} \text{ W m}^{-2} \text{ sr}^{-1}$. The same source was found in the contour plots from the other MSX bands. We designated the stronger source as A and the other as B. While the IRS1 object and the infrared nebulae are related to source A, source B is also associated with a small nebular region that shows a concentration of NIR sources, as can also be seen in Figure 4.

Since only the $8.28 \mu\text{m}$ flux density was given in the MSX *psc* for both sources, we integrated the flux density of each individual source for the four mid-infrared bands; the results are presented in table 1, which also shows the values from MSX and IRAS catalogs. Our integrated flux density for source B in the $8.28 \mu\text{m}$ coincides within 5% with the value given in the MSX catalogue, but it is 30% larger for the A source. This discrepancy can be understood if we consider that the automatic MSX algorithm subtracted part of the source B flux density as background contribution. The relative contribution of source B decreases with increasing wavelength, explaining also why it was not resolved by the MSX algorithm. It should be noticed that the reported IRAS flux density at $12 \mu\text{m}$ coincides with the sum of our derived flux densities at $12.13 \mu\text{m}$ within 10%, while the MSX value was about 50% lower.

In Figure 5 we plotted the mid to far-infrared spectral energy distribution of the sources A and B, without any correction for absorption. We assumed that the IRAS flux density in the far infrared is divided between the two sources in the same way as in the mid-infrared (14.65 and $21.33 \mu\text{m}$): about 90% originating from source A and 10% from source B. We then integrated the observed flux densities in the mid-far infrared, assuming a distance of 3.7 kpc , obtaining a luminosity $L_{\text{A}} = 8.7 \times 10^4 L_{\odot}$ and $L_{\text{B}} = 9 \times 10^3 L_{\odot}$ for sources A and B, respectively. Assuming that the IR flux density represents a lower limit for bolometric luminosity of the embedded stars, we derived ZAMS spectral types O8 and B0.5 for the sources A and B, respectively (Hanson et al.

1997).

3.2. Cluster population

In order to examine the nature of the stellar population in the direction of the IRAS source, we analyzed the stars in two delimited regions: one that we labeled "cluster", which contains the nebula and another that we labeled "control", which has a stellar population that we believe is dominated by "field" stars, as illustrated in Figure 6. We represented the position of all objects detected in the H band by crosses and we can see that the small region labeled "cluster" shows a concentration of sources. In figure 7 we present comparative $(J - H)$ versus $(H - K)$ diagrams for the stars detected in the J , H and K images, together with the position of the main sequence, giant branch and reddening vectors for early and late type stars (Koornneef 1983).

We see that the stellar population of the "cluster" region is quite different from that of the "control" region, with many sources lying on the right side of the reddening vector for early type stars, showing excess emission at $2.2 \mu\text{m}$. In the "control" region the majority of the sources have colors of reddened photospheres, with many objects located along the reddening vector for late type stars. It is well established that very young pre-main sequence objects present large infrared excess due to the presence of warm circumstellar dust (Lada & Adams 1992). Our results suggest that the stellar population in the direction of the IRAS source is very young, as can be inferred from their position in the $(J - H)$ versus $(H - K)$ diagram.

We separated the cluster sources from the field stars, by selecting all sources that lie to the right or on the reddening vector for early type stars in the cluster's color-color diagram. Table 2 shows the coordinates and photometry of all selected sources (J , H and K magnitudes from both LNA and 2MASS surveys).

Further information about the nature of the selected objects in Table 2 can be extracted from J versus $(J - H)$ color-magnitude diagram shown in Figure 8. We used this diagram instead the K versus $(H - K)$ color-magnitude diagram to minimize the effect of the "excess" of emission in the NIR on the derived stellar spectral types. The lo-

cus of the main-sequence for class V stars at 3.7 kpc (Caswell & Haynes 1987) is also plotted, with the position of each spectral type earlier than A0 V indicated. The intrinsic colors were taken from Koornneef (1983) while the absolute J magnitudes were calculated from the absolute visual luminosity for ZAMS taken from Hanson et al. (1997). The reddening vector for a ZAMS B0 V star, taken from Rieke & Lebofsky (1985), is shown by the dashed line with the positions of visual extinctions $A_V = 10$ and 20 magnitudes indicated by filled circles. We also indicated the sources with and without "excess" in the color-color diagram by open and filled triangles respectively.

For the assumed distance, we estimated the spectral type of the stars that do not present excess emission in the near infrared, by following the de-reddening vector in the color-magnitude diagram, for the others we only gave a rough classification; the results are shown in the last column of Table 2. The main source of error in the derived spectral types arises from uncertainties in the assumed cluster distance, which was derived from the velocities of the radio hydrogen recombination lines. Since the closest distance was used, the main uncertainties come from the errors in the galactic rotation curve model and related parameters. From the works of Blum et al. (1999, 2000, 2001) and Figuerêdo et al. (2002) comparing kinematic with spectroscopic distances we find that they do not differ in more than 1 kpc, in which case the change in the luminosity class would be of two sub-spectral types for early O stars and one for early B stars.

We must notice that source IRS1, which is associated with MSX source A, has an estimated spectral type of at least O5, reddened by about $A_V \approx 14$ magnitudes. Besides, there are five objects (IRS3, IRS11, IRS18, IRS21 and IRS33) associated with the mid-infrared source B; IRS3 is probably an O8 ZAMS star reddened by about $A_V = 7$ magnitudes, while the others have estimated spectral types of early-B stars. The corresponding bolometric luminosities are in agreement with the lower limits derived from the integrated mid-far infrared flux densities, corresponding to O8 and B0.5, for sources A and B respectively, as seen in section 3.1.

A lower limit to the number of Lyman-continuum photons produced in the star forming region, can

be calculated taking into account only the stars that do not show "excess" in the color-magnitude diagram (IRS1, 6, 8, 9, 10, 13, 14, 16, 20, 23, 26, 27 and 35 in Table 2). It was computed from the relation given by Hanson et al. (1997), resulting in 1.7×10^{49} photons s^{-1} . Is interesting to note that IRS1 is responsible for more than 90% of the Lyman continuum photons, being the main ionization source in the whole region.

It is also possible to obtain the number of ionizing Lyman continuum photons N_{Ly} from the radio continuum flux density given by Caswell & Haynes (1987), using the expression derived by Rubin (1968):

$$N_{Ly} = \frac{5.59 \times 10^{48} S(\nu) D^2 T_e^{-0.45} \nu^{0.1}}{1 + f_i [< He^+ / (H^+ + He^+)]} \quad (1)$$

where ν is in units of 5 GHz and f_i is the fraction of helium recombination photons that are energetic enough to ionize hydrogen. Using the values of $T_e = 4500$ K, $S(\nu) = 3.3$ Jy and $D = 3.7$ kpc taken from Caswell & Haynes (1987), we find that $f_i \approx 0$ and $N_{Ly} \sim 6 \times 10^{48}$ photons s^{-1} , compatible with the lower limit derived from the observed stars.

3.3. The Infrared Nebula

We can see from the detailed J , H and nbK images in figure 2 that the nebula presents a spheroidal shape, approximately symmetric around the IRS1 source. In figure 9 we shown contour maps of the nebular region at J , H and nbK bands obtained from our infrared images. The contours were calibrated in flux with the values starting at 0.44 (J), 1.6 (H) and 2.2×10^{-4} Jy/beam (K), with intervals of 0.37, 1.8 and 1.1×10^{-4} Jy/beam respectively. We estimated the total flux density by measuring the area between contours and multiplying by the value of the corresponding flux density per unit area, obtaining $S(J) = 0.023$ Jy, $S(H) = 0.07$ Jy and $S(K) = 0.11$ Jy. We then corrected these results for extinction, using the mean value $< A_V > = 15.1$ magnitudes, derived from the stars in the direction of the nebula that do not present infrared excess (IRS1, IRS6 and IRS10), and the standard extinction law from Rieke & Lebofski (1985). We obtained $S(J) = 1.16$ Jy, $S(H) = 0.8$ Jy and $S(K) = 0.52$ Jy.

In the previous section we showed that the number of ionizing photons available from the detected

stars is enough to explain the radio continuum flux density measured by Caswell & Haynes (1987). We will investigate now the contribution of free-free emission to the observed nebular IR flux density. Assuming constant density and temperature across the cloud and local thermodynamic equilibrium, the flux density $S(\nu)$ due to free-free emission can be written as:

$$S(\nu) = \tau_\nu B_\nu(T) \Omega \quad (2)$$

where τ_ν is the optical depth at frequency ν , $B_\nu(T)$ is the Planck function

$$B_\nu(T) = \frac{2h\nu^3}{c^2} \frac{1}{\exp(h\nu/kT) - 1} \quad (3)$$

and Ω is the solid angle of the source given by:

$$\Omega = \pi(L/2D)^2 \quad (4)$$

where L is the diameter of the ionized cloud and D the distance to the observer. The optical depth at a given frequency ν is:

$$\tau_\nu = \alpha_{\text{ff}} L \quad (5)$$

where α_{ff} is the free-free absorption coefficient (cgs) taken from Rybick (1979):

$$\alpha_{\text{ff}} = \frac{3.7 \times 10^8 [1 - \exp(-h\nu/kT)] n_e n_i g_{\text{ff}}(\nu, T)}{\nu^3 Z^{-2} T^{1/2}} \quad (6)$$

where $g_{\text{ff}}(\nu, T)$ is the Gaunt factor obtained from Karzas & Latter (1961).

For two frequencies ν_1 and ν_2 the ratio of the corresponding flux densities $S(\nu_1)$ and $S(\nu_2)$ may be calculated from:

$$\frac{S(\nu_1)}{S(\nu_2)} = \exp[h(\nu_2 - \nu_1)/kT] \frac{g_{\text{ff}}(\nu_1, T)}{g_{\text{ff}}(\nu_2, T)} \quad (7)$$

For a flux density in the 5 GHz continuum of 3.3 Jy and an electron temperature $T_e = 4500$ K, as given by Caswell & Haynes (1987) the expected flux densities at the J , H and K bands are 0.05, 0.10 and 0.16 Jy, respectively. We verify that the measured values are much larger than what was expected from the free-free emission, derived from the radio data. In fact, only an absorption as low as 4 magnitudes would explain the inferred spectrum as free-free emission. Since in the direction of the A source, this absorption is incompatible

with even the less absorbed star (IRS1), we believe that this is not the main source of extended IR emission.

Accepting the mean value of $\langle A_V \rangle = 15.1$ magnitudes as the mean value for the absorption in the direction of A source, we found that the corrected flux density increases with frequency, suggesting that the observed extended radiation is scattered light from the nearby stars. We adjusted then a black body to the NIR fluxes, obtaining a good fit for $T \approx 16000$ K, characteristic of middle-B stars (Hanson et al. 1997). Lumsden & Puxley (1996), analyzing the ultracompact HII region G45.12+0.13, also obtained an extinction corrected flux density that increases with decreasing wavelengths and interpreted it as due to stellar light, scattered by dust through the HII region.

3.4. Conclusions

Near-IR imaging in the direction of the CS molecular cloud associated with the IRAS source 16132-5039, revealed an embedded young massive stellar cluster. We detected 35 member candidates up to our completeness limit, concentrated in an area of about 2 square parsec. All images, but especially the H and nbK bands, show the presence of a small spheroidal nebula with a bright star (IRS1) at its center.

The stars associated with the IRAS point source were identified using more accurate positions from the MSX catalogue. The analysis of the mid-infrared images revealed that there are two sources associated with IRAS 16132-5039. The strongest coincides with the position of at least a dozen of OB stars, while the weaker source is associated to less massive objects, with spectral types characteristic of middle-B ZAMS stars. The integral of the spectral energy distribution of the MSX-IRAS sources, between 8.28 μm and 100 μm , gives lower limits to the bolometric luminosity of the embeded objects of $L = 8.7 \times 10^4 L_\odot$ and $L = 9 \times 10^3 L_\odot$, which corresponds to ZAMS O8 and B0.5 stars, respectively (Hanson et al. 1997). The results are compatible with the spectral types of the objects detected in the NIR, since it is possible that only part of the energy emitted by the stars is reprocessed by the dusty envelope. In that sense, they can be taken as lower limits to the bolometric luminosity of the embeded stars.

Assuming that the radio emission measured by Caswell & Haynes (1987) originates in this region, at a distance of 3.7 kpc, we estimated the number of ionizing Lyman continuum photons as $N_{Ly} \sim 6 \times 10^{48}$ photons s^{-1} . On the other hand, the number of Lyman continuum photons expected from the stars that lie along the reddening line for early-type stars is about 1.7×10^{49} s^{-1} , enough to produce the detected flux densities at 5 GHz. The IRS1 source is enough to account for more than 90% of the total number of Lyman continuum photons necessary to ionize the gas.

Analysis of the integrated flux densities of the NIR nebula at the J , H and nbK bands revealed that they increase with frequency, implying that free-free emission cannot be the main source of the extended luminosity, unless we assume only four magnitudes of visual extinction. Since this value is incompatible with the extinction derived from the stars that do not shown excess of emission at $2.2 \mu m$, we conclude that the observed emission must be mainly dust scattered light.

A comparison of the cluster described in this paper with the young stellar cluster associated with the IRAS source 16177-5018 (Roman-Lopes et al. 2003), which is located at the same distance and direction, shows that the the former contains less massive stars. Since its mean visual absorption is also about 10 magnitudes smaller than that of IRAS 16177-5018, it is possible that it was formed from a less massive molecular cloud.

This work was partially supported by the Brazilian agencies FAPESP and CNPq. We acknowledge the staff of Laboratório Nacional de Astrofísica for their efficient support and to Anderson Caproni by help during the observations. This publication makes use of data products from the Two Micron All Sky Survey, which is a joint project of the University of Massachusetts and the Infrared Processing and Analysis Center/California Institute of Technology, funded by the National Aeronautics and Space Administration and the National Science Foundation. This research made use of data products from the Mid-course Space Experiment.

REFERENCES

- Blum, R. D., Daminieli, A., Conti, P. S. 1999, *AJ*, 117, 1392
- Blum, R. D., Conti, P. S., Daminieli, A. 2000, *AJ*, 119, 1860
- Blum, R. D., Daminieli, A., Conti, P. S. 2001, *AJ*, 121, 3149
- Bronfman, L. Nyman, L. A., May, J. 1996, *A&AS*, 115, 81
- Caswell, J. L., Haynes, R. F. 1987, *A&A*, 171, 261
- Dutra, C. M., Bica, E., Soares, J., Barbuy, B. 2003, *A&A*, 400, 533
- Egan, M. P., Dyk, S. D. V., Price, S. D. 2001, *AJ*, 122, 1844
- Elias, J. H. 1982, *AJ*, 87, 1029
- Figuerêdo, E., Blum, R. D., Daminieli, A., Conti, P. S. 2002, *AJ*, 124, 2739
- Hanson, M. M., Howarth, I. D., Conti, P. S. 1997, *ApJ*, 489, 718
- Iben, I. Jr. 1965, *ApJ*, 141, 993I
- Karzas, W. J., Latter, R. 1961, *ApJ*, 6, 167
- Koornneef, J. 1983, *A&A*, 128, 84
- Lada, C. J., Adams, F. C. 1992, *ApJ*, 393, 278
- Lumsden, S. L., Puxley, P. J. 1996, *MNRAS*, 281, 493
- Price, S. D., Egan, M. P., Carey, S. J., Mizuno, D. R., Kuchar, T. A. 2001, *AJ*, 121, 2819
- Rieke, G. H., Lebofsky, M. J. 1985, *ApJ*, 288, 618
- Roman-Lopes, A., Abraham, Z., Caproni, A., Lépine, J. R. D. 2002, *IAUS*, 206, 244
- Roman-Lopes, A., Abraham, Z., Lépine, J. R. D. 2003, *AJ*, 126, 1896
- Rubin, R. H. 1968, *ApJ*, 154, 391R
- Rybicki, G. B., Lightman, A. P. 1979, *Radiative Processes in Astrophysics*, ed. JOHN WILEY & SONS, New York

Simpson, J. P., Rubin, R. H. 1990, ApJ, 354, 165

Spitzer, L. 1978, Physical Processes in the Interstellar Medium, ed. Wiley, New York

Stetson, P. B., 1987, PASP, 99, 191

Persi, P. Tapia, M., Roth, M. 2000, A&A357, 1020

Wood, D. O. S., Churchwell, E. 1989, ApJ, 340, 265

TABLE 1

INTEGRATED FLUXES FROM MSX *A, C, D* AND *E* IMAGES FOR THE TWO MID-INFRARED SOURCES (SEE TEXT). ALSO ARE SHOWN THE DATA FROM MSX AND IRAS POINT SOURCE CATALOGUE (*psc*).

| $\lambda(\mu\text{m})$ | Integration "A" | Integration "B" | MSX <i>psc</i> "A" | MSX <i>psc</i> "B" | IRAS <i>psc</i> |
|------------------------|-----------------|-----------------|--------------------|--------------------|-----------------|
| 8.28 | 15.8 | 4.3 | 11.3 | 4.1 | ... |
| 12 | ... | ... | ... | ... | 44.8 |
| 12.13 | 32.8 | 3.6 | 23.0 | ... | ... |
| 14.65 | 23.9 | 2.0 | 21.3 | ... | ... |
| 21.33 | 117 | 10.8 | 123.8 | ... | ... |
| 25 | ... | ... | ... | ... | 266 |
| 60 | ... | ... | ... | ... | 2311 |
| 100 | ... | ... | ... | ... | 4618 |

TABLE 2
LIST OF THE SELECTED NEAR-INFRARED SOURCES

| IRS | α (J2000) | δ (J2000) | J_{CamIV} | J_{2mass} | H_{CamIV} | H_{2mass} | K_{CamIV} | K_{2mass} | <i>Spec Type</i> |
|-----|------------------|------------------|-------------|-------------|-------------|-------------|-------------|-------------|------------------|
| 1 | 16:17:02.20 | -50:47:03.1 | 12.26(4) | 11.97(4) | 10.88(4) | 10.65(4) | 10.07(4) | 9.73(4) | O5 |
| 2 | 16:17:09.23 | -50:47:14.7 | 13.36(3) | 13.26(4) | 11.66(2) | 11.47(3) | 10.13(3) | 10.15(3) | mid-O |
| 3 | 16:16:55.8 | -50:47:23 | 11.77(2) | ... | 11.01(2) | ... | 10.30(4) | ... | early-B |
| 4 | 16:17:00.62 | -50:47:49.6 | 12.47(1) | ... | 12.02(2) | ... | 11.17(4) | 10.92(2) | early-B |
| 5 | 16:17:02.63 | -50:46:56.6 | 14.43(3) | 14.26(8) | 12.78(3) | 12.51(7) | 11.64(4) | 11.17(7) | early-B |
| 6 | 16:17:03.7 | -50:47:05 | 14.61(3) | ... | 13.04(2) | ... | 12.03(5) | ... | B0 |
| 7 | 16:17:02.88 | -50:47:05.1 | 17.08(9) | ... | 14.84(6) | ... | 11.55(5) | 11.62(7) | early-B |
| 8 | 16:17:06.30 | -50:47:09.3 | 13.23(2) | 13.31(3) | 12.28(3) | 12.34(3) | 11.42(3) | 11.70(3) | B0 |
| 9 | 16:17:04.37 | -50:47:16.4 | 13.28(2) | 13.26(2) | 12.44(2) | 12.45(3) | 11.64(3) | 11.78(5) | B0.5 |
| 10 | 16:17:03.72 | -50:47:15.7 | 13.86(3) | 13.92(4) | 12.57(3) | 12.69(4) | 11.80(4) | 11.92(5) | B0 |
| 11 | 16:16:56.0 | -50:47:22 | 13.12(3) | ... | 12.62(4) | ... | 12.06 | ... | early-B |
| 12 | 16:16:59.72 | -50:47:47.0 | 17.32(10) | ... | 14.76(6) | ... | 12.25(5) | 12.31(6) | early-B |
| 13 | 16:17:02.06 | -50:47:26.6 | 16.27(6) | ... | 13.95(6) | ... | 12.54(5) | 12.60(9) | O9.5 |
| 14 | 16:17:08.61 | -50:47:11.5 | 15.39(5) | ... | 13.76(3) | 13.65(6) | 12.64(9) | 12.65(2) | B0.5 |
| 15 | 16:17:02.0 | -50:47:01 | 16.23(6) | ... | 14.35(4) | ... | 12.51(6) | ... | early-B |
| 16 | 16:17:04.16 | -50:47:49.8 | 13.89(3) | ... | 13.27(3) | ... | 12.87(6) | 12.72(7) | B2 |
| 17 | 16:17:03.13 | -50:47:15.4 | 14.74(3) | 14.61(6) | 13.65(3) | 13.57(5) | 12.71(6) | 12.73(7) | early-B |
| 18 | 16:16:55.6 | -50:47:28 | 15.74(5) | ... | 14.24(4) | ... | 12.61(6) | ... | early-B |
| 19 | 16:17:03.7 | -50:47:08 | 15.53(5) | ... | 13.91(4) | ... | 12.69(7) | ... | early-B |
| 20 | 16:17:02.02 | -50:48:12.1 | 14.94(3) | 14.90(5) | 13.89(4) | 13.71(5) | 12.55(7) | 12.88(5) | B2 |
| 21 | 16:16:55.3 | -50:47:25 | 16.22(8) | ... | 14.56(5) | ... | 12.95(6) | ... | early-B |
| 22 | 16:17:02.5 | -50:46:54 | 16.35(8) | ... | 14.47(5) | ... | 12.98(6) | ... | early-B |
| 23 | 16:17:03.93 | -50:47:34.0 | 16.50(7) | ... | 14.42(4) | 14.42(8) | 13.31(7) | 13.20(5) | B0.5 |
| 24 | 16:17:03.9 | -50:47:13 | 18.17(18) | ... | 15.16(7) | ... | 13.12(6) | ... | early-B |
| 25 | 16:16:59.41 | -50:47:52.9 | 17.16(9) | ... | 15.04(5) | ... | 13.11(6) | 13.31(7) | early-B |
| 26 | 16:17:08.12 | -50:47:37.4 | 16.21(6) | ... | 14.47(4) | 14.51(7) | 13.29(8) | 13.38(6) | B2 |
| 27 | 16:17:02.12 | -50:47:37.2 | 16.54(8) | ... | 14.50(4) | ... | 13.42(7) | 13.40(11) | B1 |
| 28 | 16:17:03.8 | -50:47:11 | 17.40(11) | ... | 15.36(6) | ... | 13.32(7) | ... | early-B |
| 29 | 16:17:02.2 | -50:47:35 | 16.63(7) | ... | 14.86(7) | ... | 13.61(7) | ... | early-B |
| 30 | 16:17:03.88 | -50:48:16.0 | 16.08(7) | 15.59(9) | 15.54(7) | 14.69(9) | ... | 13.74(8) | mid-B |
| 31 | 16:17:05.23 | -50:47:31.7 | 15.28(4) | 15.20(9) | 14.63(5) | ... | 13.53(5) | 13.87(8) | ... |
| 32 | 16:17:06.74 | -50:48:05.2 | 16.16(7) | 15.85(8) | 15.37(6) | ... | ... | 14.18(10) | ... |
| 33 | 16:16:55.9 | -50:47:20 | 13.62(5) | ... | 12.93(4) | ... | 11.90(4) | ... | early-B |
| 34 | 16:17:03.8 | -50:47:47 | 16.42(6) | ... | 14.25(5) | ... | 12.85(6) | ... | B0 |
| 35 | 16:17:03.5 | -50:47:03 | 15.67(5) | ... | 13.79(4) | ... | 12.56(6) | ... | B0.5 |

*Stars that show "excess" of emission at 2.2 μ m

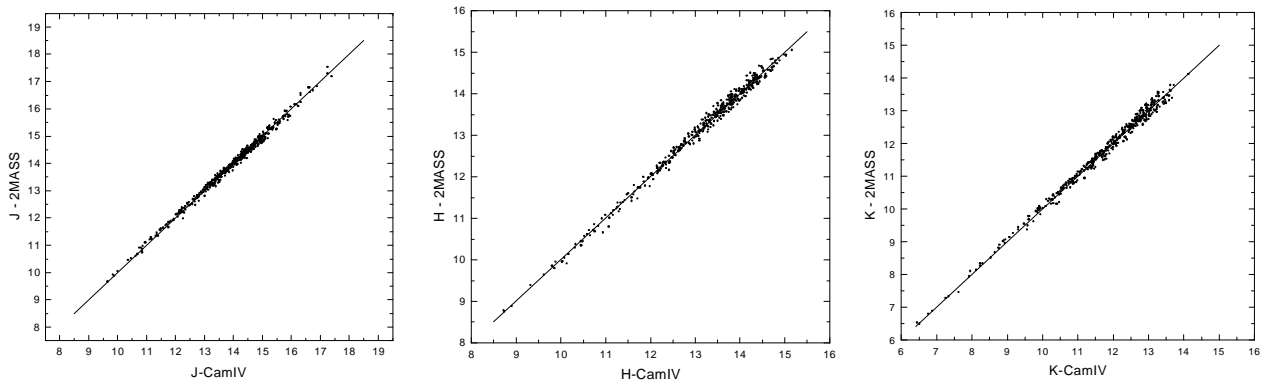


Fig. 1.— Magnitudes comparative diagram $M_{JHK}(2MASS) \times M_{JHK}(CamIV)$. The continuous line shows the relation expected if the two photometric systems were equal.

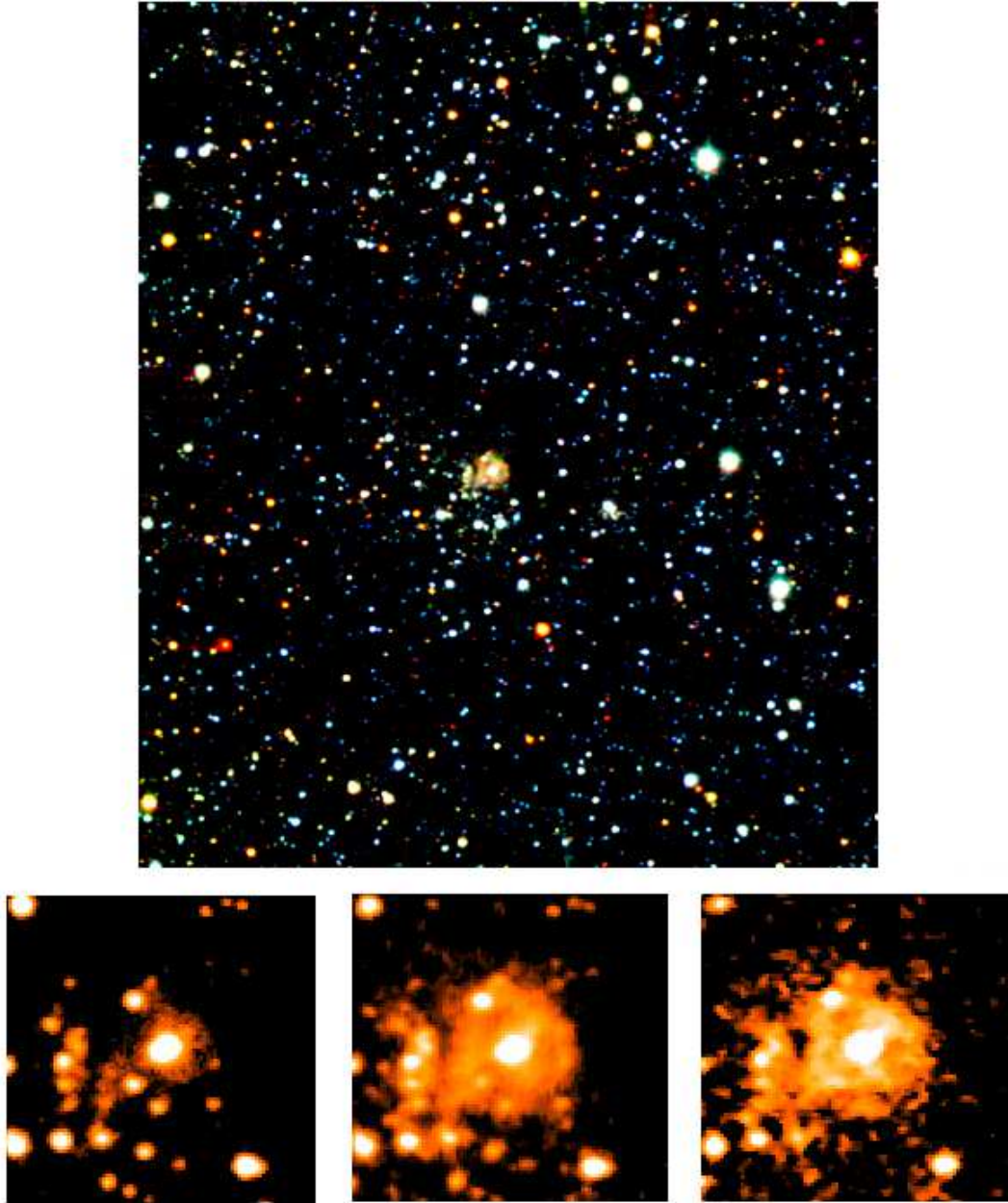


Fig. 2.— Combined false-image made from the J , H and nbK LNA images. North is to the top east to the right. At the bottom are detailed views of the infrared nebulae J (*left*), H (*center*) and nbK (*right*) images.

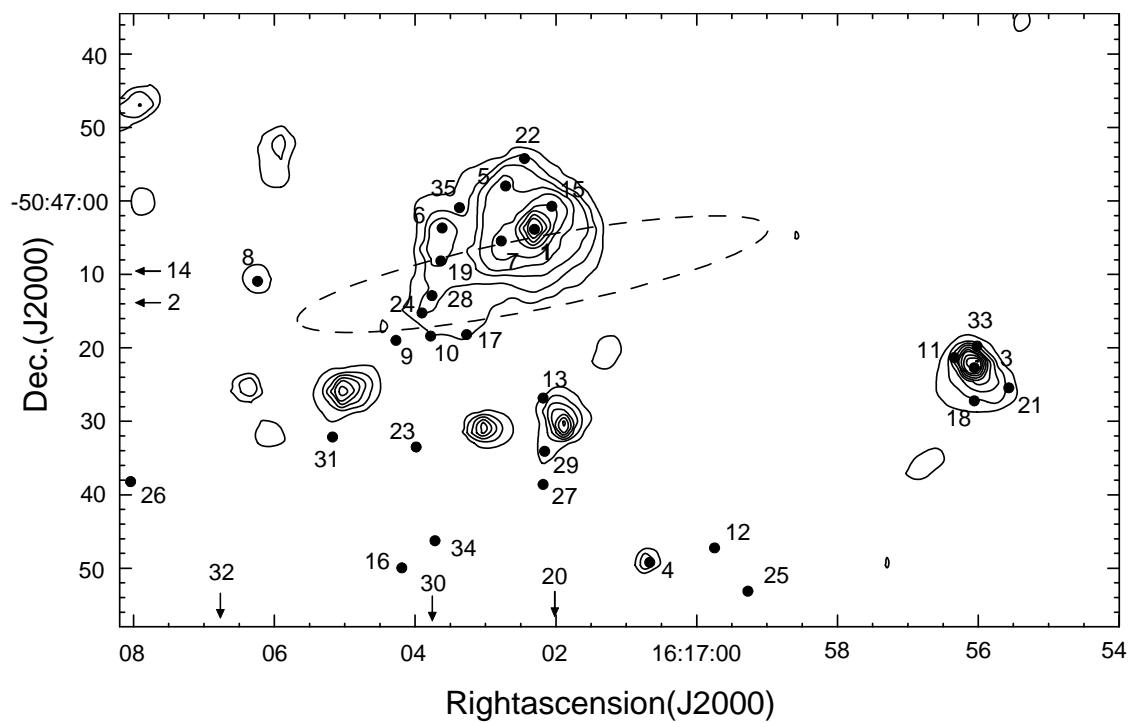


Fig. 3.— nbK band contour map of the infrared nebulae associated with IRAS 16132-5039. The contours start at 2.2×10^{-4} Jy/beam, with the same intervals (the beam size is 2×2 pixels). The positions of selected infrared sources referred in Table 2 and the IRAS coordinate ellipse error (dotted line) also are indicated.

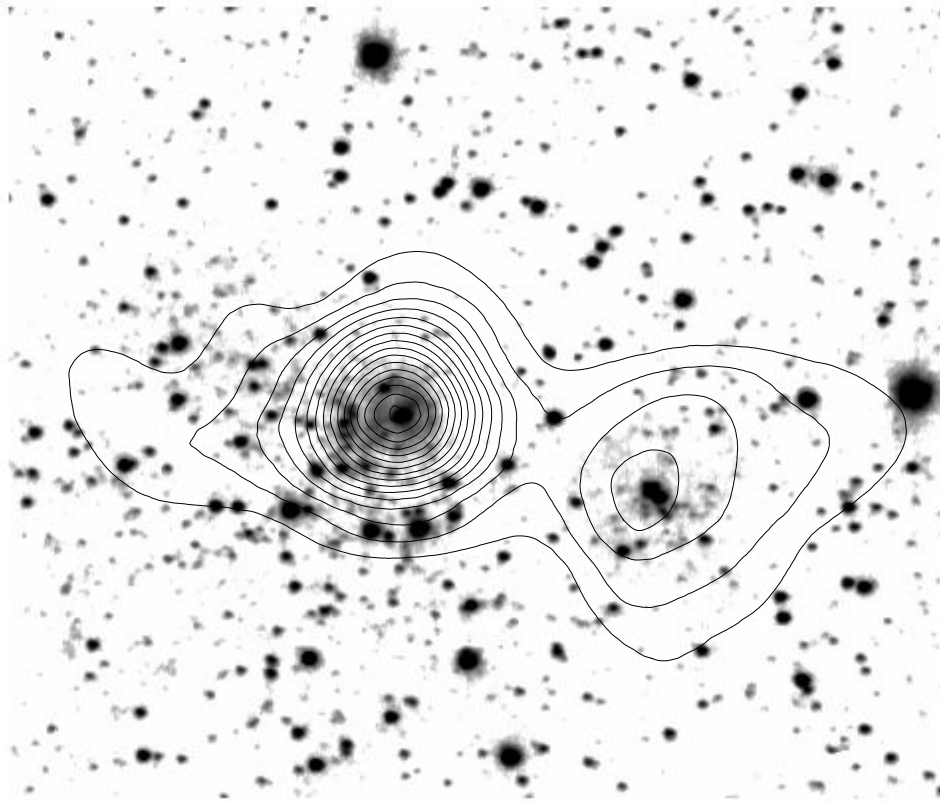


Fig. 4.— Contour diagram from the *A* MSX band image ($8.28\mu\text{m}$), overlaying a LNA's *H* band image. The contours start at $2.8 \times 10^{-5} \text{ W/m}^2\text{sr}$ and are spaced by $8 \times 10^{-6} \text{ W/m}^2\text{sr}$.

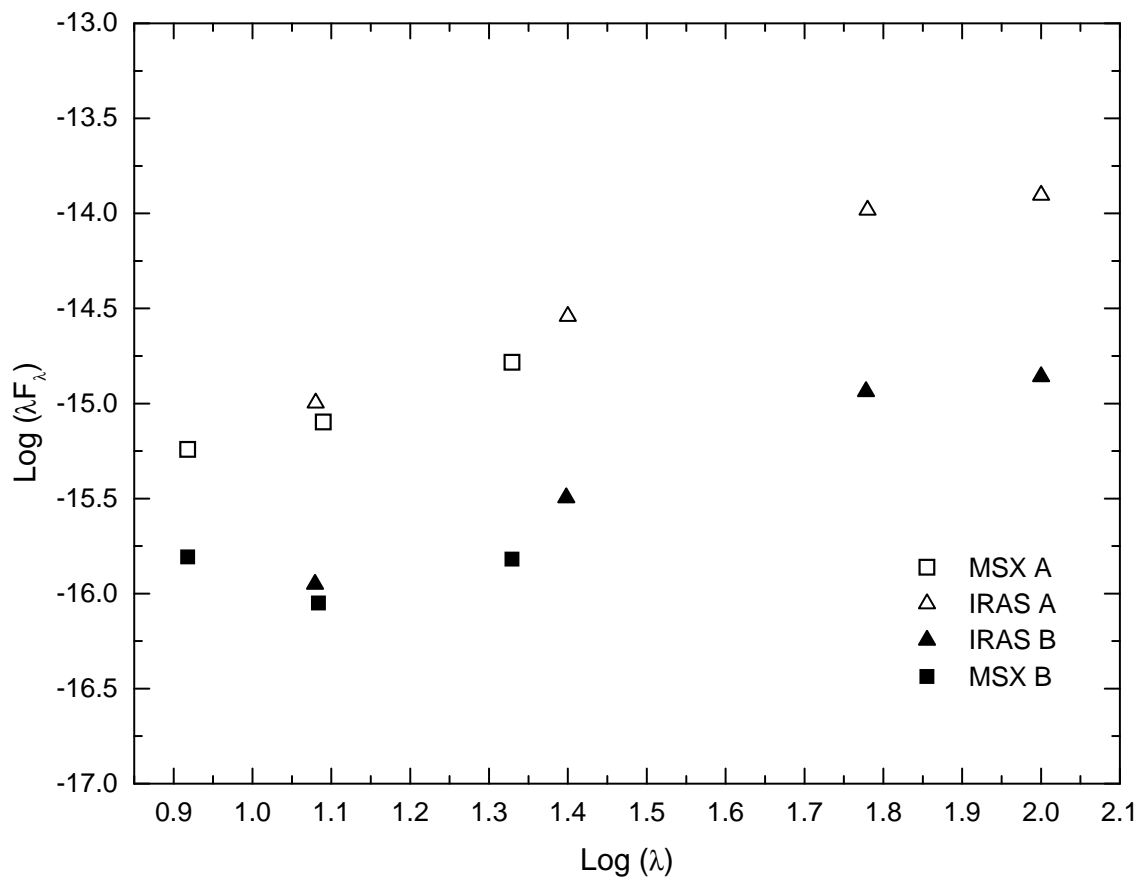


Fig. 5.— Spectral energy distribution of the "A" and "B" MSX sources. The mid infrared data (squares) were obtained from the integrated flux of the individual sources in the MSX images (bands A=8.28 μ m, C=12.13 μ m, D=14.65 μ m and E=21.34 μ m) while the far infrared data (triangles) were taken from IRAS, and are listed in Table 1.

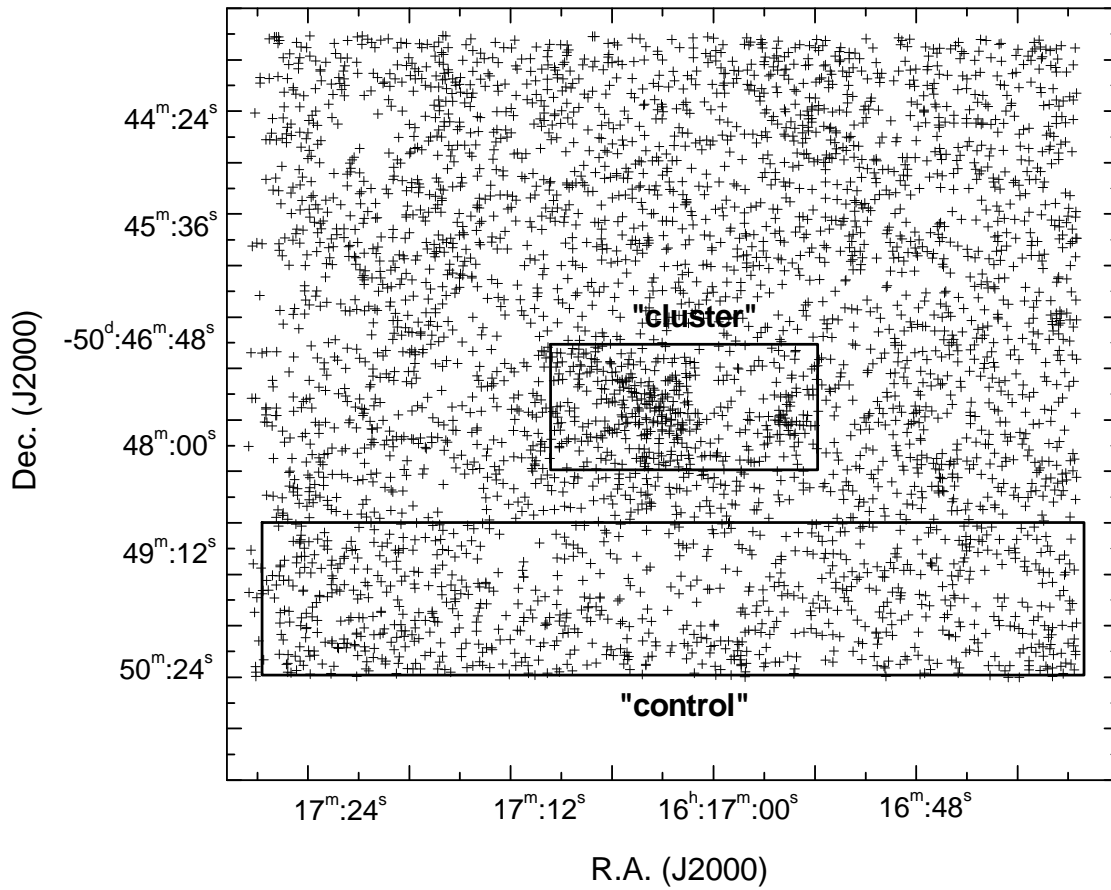


Fig. 6.— Diagram of the spacial distribution of sources detected at LNA's H band image. The two regions (a) (cluster) and (b) (control) are delimited by boxes .

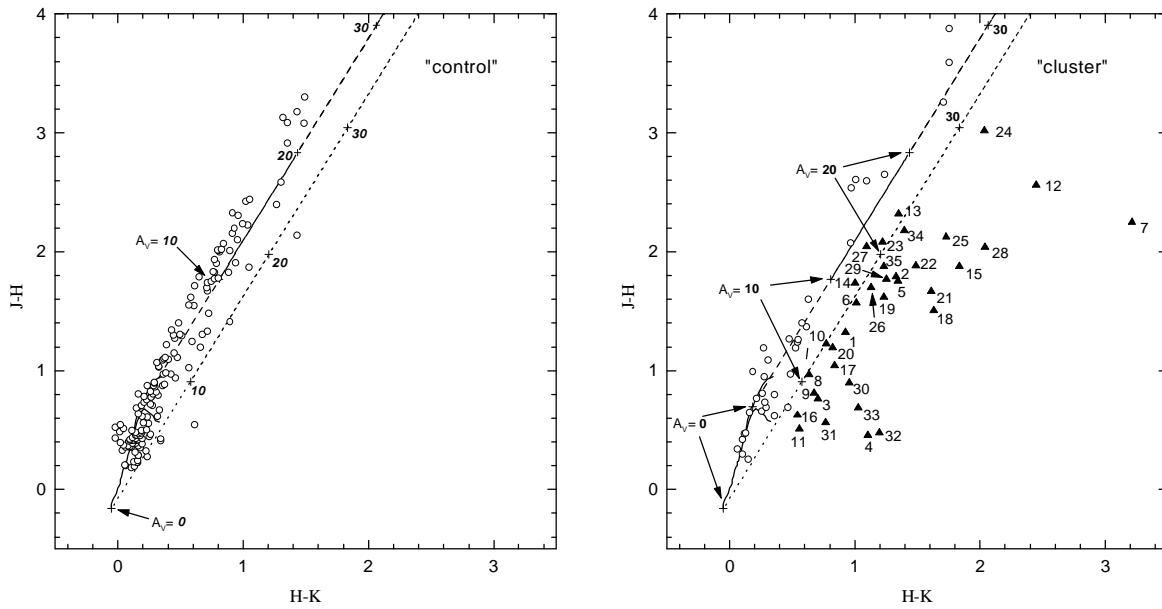


Fig. 7.— Color-color diagrams for two regions in our survey. The region labeled "control" (left panel) contains only foreground objects; the other labeled "cluster" (right panel) has also a foreground population (open circles) but presents objects with infrared "excess" (filled triangles). All objects with "excess" are located in the "cluster area". The locus of the main sequence and giants branch are shown by the continuous lines taken from Koornneef (1983), while the dashed and dotted lines follow the reddening vectors taken from Rieke & Lebofsky (1985). The location (plus signs) of $A_V = 0, 10, 20$ magnitudes of visual extinction also are indicated. The cluster members candidates are labeled by numbers.

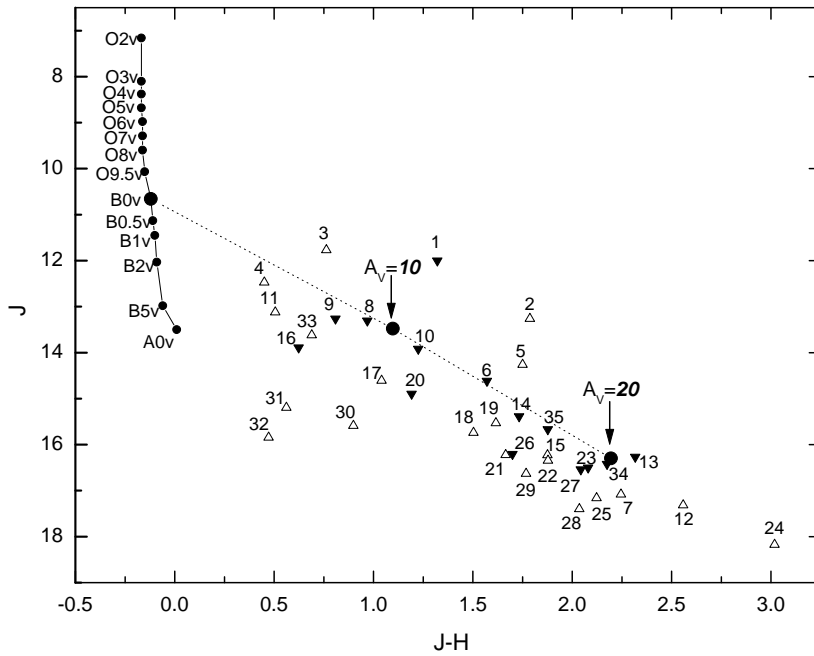


Fig. 8.— The J versus $(J - H)$ color-magnitude diagram of the sources in table 2. The locus of the main sequence at 3.7 kpc is shown by the continuous line. The intrinsic colors were taken from Koornneef (1983) while the absolute J magnitudes were calculated from the absolute visual luminosity for ZAMS taken from Hanson et al. (1997). The reddening vector for a B0 ZAMS star (dotted line) was taken from Rieke & Lebofsky (1985). We also indicated the location (bold numbers) of $A_V = 10$ and 20 magnitudes of visual extinction as well as the sources that show "excess" (open up triangles) and do not (filled down triangles) in the color-color diagram.

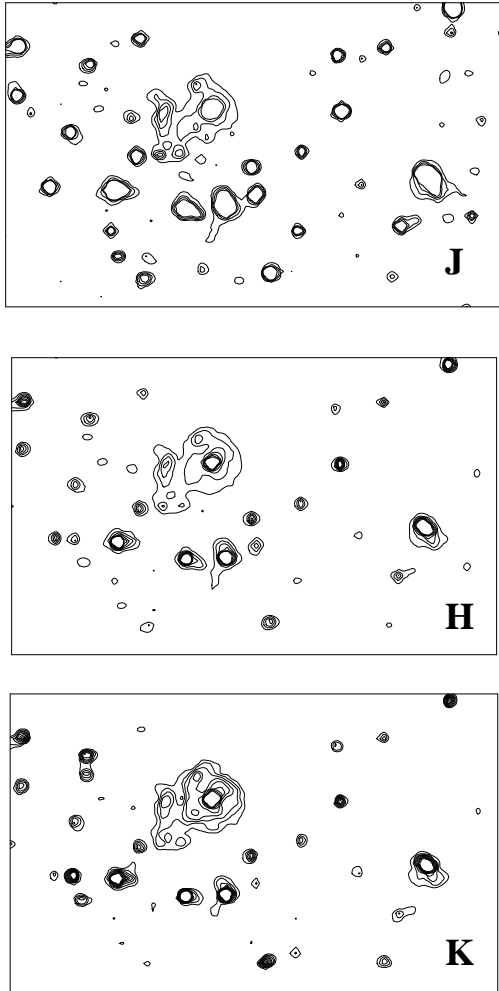


Fig. 9.— The J , H and nbK contour maps of the infrared nebula region. The contours start at 0.44 (J), 1.6 (H) and 2.2×10^{-4} Jy/beam (K), and are spaced by 0.37, 1.8 and 1.1×10^{-4} Jy/beam respectively.